CrossMark

J. Fluid Mech. (2021), *vol*. 929, R3, doi:10.1017/jfm.2021.903



Shock-induced dual-layer evolution

Yu Liang[1,2] **and Xisheng Luo**[2,†]

[1]NYUAD Research Institute, New York University Abu Dhabi, Abu Dhabi 129188, UAE

[2]Advanced Propulsion Laboratory, Department of Modern Mechanics, University of Science and Technology of China, Hefei 230026, PR China

(Received 12 September 2021; revised 3 October 2021; accepted 8 October 2021)

Shock-induced fluid-layer evolution has attracted much attention but remains a challenge mainly because the coupling between layers remains unknown. Linear solutions are first derived to quantify the layer-coupling effect on the shocked dual-layer evolution. Next, the motions of the waves and interfaces of a dual layer are examined based on the one-dimensional gas dynamics theory. Shock-tube experiments on the dual-layer, single-layer and single-mode interface are then performed to validate the linear solutions and investigate the reverberating waves inside the layers. It is proved that the layer-coupling effect destabilises the dual layer, especially when the initial layers are thin, and the reverberating waves impose additional instabilities on all interfaces. Our findings suggest that a slow/fast configuration with a large thickness in a dual layer can facilitate the suppression of hydrodynamic instabilities.

Key words: shock waves

1. Introduction

Rayleigh–Taylor instability (RTI) develops when a light fluid accelerates a heavy fluid (Rayleigh 1883; Taylor 1950), then bubbles (light fluids penetrating heavy ones) and spikes (heavy fluids penetrating light ones) arise, and finally a flow transition to turbulence might occur (Zhou *et al.* 2019). A similar phenomenon is observed in Richtmyer–Meshkov instability (RMI) (Richtmyer 1960; Meshkov 1969), which occurs when an interface separating two kinds of fluids is impulsively accelerated by a shock wave. Both instabilities play essential roles in various industrial and scientific fields, such as inertial confinement fusion (ICF) (Lindl *et al.* 2014) and supernova explosion (Kuranz *et al.* 2018). For example, a typical ICF capsule contains the outer ablator layer, the middle push layer and the inner fuel layer. An RMI occurs when the shocks generated by intense lasers or X-rays interact with these multiple layers, determining the seed of RTI during the implosion

† Email address for correspondence: xluo@ustc.edu.cn

© The Author(s), 2021. Published by Cambridge University Press

https://doi.org/10.1017/jfm.2021.903 Published online by Cambridge University Press

(Goncharov 1999). The mixing induced by RMI and RTI significantly reduces and even eliminates the thermonuclear yield (Miles *et al.* 2004; Qiao & Lan 2021). In addition, the shocks generated by star collapse in a supernova interact with multilayer heavy elements throughout the interstellar space. The mixing induced by RMI and RTI shapes the filament structures in the remnant of the historical supernova of 1054 AD. Therefore, understanding the RMI and RTI of a finite-thickness fluid layer is significant.

Most previous works focused on the evolution of a single-mode interface induced by these two instabilities (Sharp 1984; Brouillette 2002; Zhou 2017*a*,*b*; Zhai *et al.* 2018) and there are only a few exceptions on a single fluid layer. Theoretically, Taylor (1950) was the first to consider the RTI of a liquid layer and found that the interface-coupling effect is significant when the initial layer is sufficiently thin. Subsequently, Ott (1972) proposed a nonlinear solution describing the RTI of a thin massless fluid layer and explained the formation of bubbles and spikes. Mikaelian (1985, 1993, 1996) and Jacobs *et al.* (1995) separately derived the linear solutions for the RMI of an A/B/A-type fluid layer. Experimentally, gas curtain technology was adopted to explore the RMI of a thin SF_6 layer surrounded by air. It was found that the SF_6 layer morphologies are sensitive to its initial shape (Jacobs *et al.* 1993; Budzinski, Benjamin & Jacobs 1994; Jacobs *et al.* 1995; Rightley, Vorobieff & Benjamin 1997), and the late-time mixing is influenced by initial conditions such as the perturbation amplitude and wavelength (Prestridge *et al.* 2000; Tomkins *et al.* 2008; Balakumar *et al.* 2012; Orlicz, Balasubramanian & Prestridge 2013). In addition, the soap-film technique was recently utilised to generate an initial shape-controllable and layer-thickness-controllable SF_6 gas layer surrounded by air (Ding *et al.* 2019; Liang *et al.* 2020; Sun *et al.* 2020; Liang & Luo 2021). It was figured out that the waves reverberating inside a fluid layer impose various interfacial instabilities on the two interfaces of the layer (Liang *et al.* 2020; Liang & Luo 2021).

However, multiple layers are more general in applications. For example, the double-shell ICF capsule consists of a plastic form shell (35 mg cm^{-3}) between the outer shell (2.7 g cm^{-3}) and the inner shell (200 mg cm^{-3}) (Montgomery *et al.* 2018; Haines *et al.* 2021). The heavy elements throughout the interstellar space in the supernova are also multilayered (Kuranz *et al.* 2018). The influence of the coupling between layers on the interfacial instabilities remains unknown. In addition, due to more waves reverberating inside a shocked multilayer, it is expected that the additional instabilities induced by these waves are different under the single-layer and multilayer conditions.

In this study, we first theoretically deduce analytical, linear solutions for the RMI of a dual layer (three interfaces), which are also applicable to the semi-infinite (one interface) and single-layer (two interfaces) RMI. Then, we examine the influences of the reverberating waves on the motions of all interfaces of a dual layer. Later, we validate our analytical solutions with quasi-two-dimensional (quasi-2-D) RMI experiments on dual-layer, single-layer and single-mode interface evolutions. Finally, the layer-coupling effect on the RMI is discussed, and the influences of the reverberating waves on the dual-layer evolution are quantified.

2. Linear stability analysis

In general, a dual layer contains four fluids and three interfaces. Although it is the simplest multilayer, it is still too complex to find analytical solutions, as pointed out by Mikaelian (1985), who showed that analytical solutions could not be derived when the number of fluids is larger than three and the number of interfaces is larger than two. To solve this problem, we consider a simplified system that consists of two incompressible and initially

https://doi.org/10.1017/jfm.2021.903 Published online by Cambridge University Press

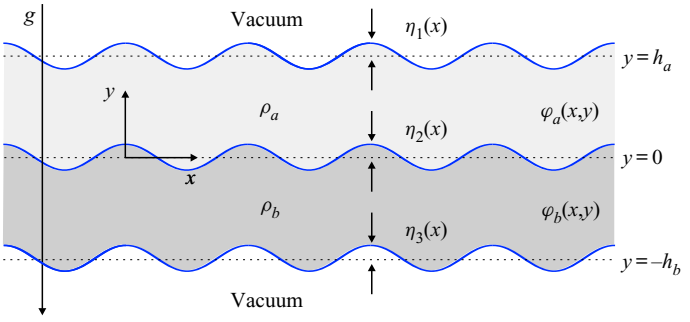


Figure 1. The configuration of the dual-layer system that consists of two incompressible and initially irrotational fluids and three nearly planar interfaces with perturbations η_1, η_2 and η_3, in a vacuum, with gravitation g. Fluid with density ρ_a, velocity potential ϕ_a and thickness h_a is overlapped on another fluid with density ρ_b, velocity potential ϕ_b and thickness h_b.

irrotational fluids and three nearly planar interfaces with single-mode perturbations η_1, η_2 and η_3, in a vacuum, with gravitation g (Guo *et al.* 2017; Liu *et al.* 2018*b*), as shown in figure 1, and which resembles the outer ablator layer and the middle push layer of an ICF capsule. Fluid with density ρ_a, velocity potential ϕ_a and thickness h_a is overlapped on another fluid with density ρ_b, velocity potential ϕ_b and thickness h_b. The velocity potentials ϕ_a and ϕ_b satisfy

$$\nabla^2\phi = 0. \tag{2.1}$$

To obtain a linear solution, the periodic small perturbation amplitudes set on the first interface (a_1), second interface (a_2) and third interface (a_3) are of the form

$$\eta_1 = a_1(t)\cos(kx), \quad \eta_2 = a_2(t)\cos(kx), \quad \eta_3 = a_3(t)\cos(kx). \tag{2.2a–c}$$

The first (respectively third) interface is a free boundary located at $y = \eta_1 + h_a$ (respectively $y = \eta_3 - h_b$), and the second interface is at $y = \eta_2$ with vertical velocity being continuous. Then the kinematic conditions on the boundaries are

$$\left.\begin{aligned}
\frac{\partial\eta_1}{\partial t} + \frac{\partial\eta_1}{\partial x}\frac{\partial\phi_a}{\partial x} - \frac{\partial\phi_a}{\partial y} = 0, \quad & \text{at } y = \eta_1 + h_a,\\
\frac{\partial\eta_2}{\partial t} + \frac{\partial\eta_2}{\partial x}\frac{\partial\phi_a}{\partial x} - \frac{\partial\phi_a}{\partial y} = 0, \quad & \text{at } y = \eta_2,\\
\frac{\partial\eta_3}{\partial t} + \frac{\partial\eta_3}{\partial x}\frac{\partial\phi_b}{\partial x} - \frac{\partial\phi_b}{\partial y} = 0, \quad & \text{at } y = \eta_3 - h_b,\\
\frac{\partial\eta_2}{\partial t} + \frac{\partial\eta_2}{\partial x}\frac{\partial\phi_b}{\partial x} - \frac{\partial\phi_b}{\partial y} = 0, \quad & \text{at } y = \eta_2,
\end{aligned}\right\} \tag{2.3}$$

and the conditions of the pressure equilibrium are

$$\left.\begin{aligned}
\frac{\partial\phi_a}{\partial t} + \frac{(\nabla\phi_a)^2}{2} + g\eta_1 = 0, \quad & \text{at } y = \eta_1 + h_a,\\
\frac{\partial\phi_b}{\partial t} + \frac{(\nabla\phi_b)^2}{2} + g\eta_3 = 0, \quad & \text{at } y = \eta_3 - h_b,\\
\rho_a\left[\frac{\partial\phi_a}{\partial t} + \frac{(\nabla\phi_a)^2}{2} + g\eta_2\right] = \rho_b\left[\frac{\partial\phi_b}{\partial t} + \frac{(\nabla\phi_b)^2}{2} + g\eta_2\right], \quad & \text{at } y = \eta_2.
\end{aligned}\right\} \tag{2.4}$$

https://doi.org/10.1017/jfm.2021.903 Published online by Cambridge University Press

Combining the above equations, linearising the equations by neglecting the products $(\partial\eta/\partial x)(\partial\phi/\partial x)$ and terms $(\nabla\phi)^2$, and replacing the acceleration g by the product of the post-shock flow speed (Δv) and a Dirac delta function, the linear solutions for the amplitude growth rates of the first interface $(\dot{a}_1^l)$, second interface $(\dot{a}_2^l)$ and third interface $(\dot{a}_3^l)$ induced by RMI can be obtained as

$$\begin{aligned}\dot{a}_1^l = {} & \frac{k\Delta v\, a_2(0)}{1-\alpha^2\beta^2+\alpha\xi_1(\beta^2-1)+\beta\xi_2(\alpha^2-1)}\{\epsilon_1(\beta\xi_2-1)+\xi_1(1-\beta\epsilon_3)\\ & +\alpha\beta(\epsilon_3-\xi_2)-A\xi_1[1-\alpha^2\beta^2-\alpha(\epsilon_1-\alpha\beta\epsilon_3)-\beta(\epsilon_3-\alpha\beta\epsilon_1)]\\ & +\alpha\beta[\epsilon_3(1-\alpha\xi_1)-\alpha\beta(\epsilon_1-\xi_1)-\xi_2(1-\alpha\epsilon_1)]\},\end{aligned} \tag{2.5}$$

$$\begin{aligned}\dot{a}_2^l = {} & \frac{k\Delta v\, a_2(0)}{1-\alpha^2\beta^2+\alpha\xi_1(\beta^2-1)+\beta\xi_2(\alpha^2-1)}\{A[\alpha^2\beta^2-1+\alpha(\epsilon_1-\alpha\beta\epsilon_3)\\ & +\beta(\epsilon_3-\alpha\beta\epsilon_1)]-\alpha[\epsilon_1(1-\beta\xi_2)-\xi_1(1-\beta\epsilon_3)-\alpha\beta(\epsilon_3-\xi_2)]\\ & +\beta[\epsilon_3(1-\alpha\xi_1)-\alpha\beta(\epsilon_1-\xi_1)-\xi_2(1-\alpha\epsilon_1)]\},\end{aligned} \tag{2.6}$$

$$\begin{aligned}\dot{a}_3^l = {} & \frac{k\Delta v\, a_2(0)}{1-\alpha^2\beta^2+\alpha\xi_1(\beta^2-1)+\beta\xi_2(\alpha^2-1)}\{\epsilon_3(1-\alpha\xi_1)-\alpha\beta(\epsilon_1-\xi_1)\\ & -\xi_2(1-\alpha\epsilon_1)-A\xi_2[1-\alpha^2\beta^2-\alpha(\epsilon_1-\alpha\beta\epsilon_3)-\beta(\epsilon_3-\alpha\beta\epsilon_1)]\\ & -\alpha\beta[\epsilon_1(1-\beta\xi_2)-\alpha\beta(\epsilon_3-\xi_2)-\xi_1(1-\beta\epsilon_3)]\}.\end{aligned} \tag{2.7}$$

Here $A=(\rho_b-\rho_a)/(\rho_b+\rho_a)$ is the Atwood number of the inner interface (i.e. the second interface), $\alpha=\mathrm{e}^{-kh_a}$, $\beta=\mathrm{e}^{-kh_b}$, $\xi_1=-2\alpha(1-\beta^2)A/[(1-\alpha^2\beta^2)(1-A)]$, $\xi_2=2\beta(1-\alpha^2)A/[(1-\alpha^2\beta^2)(1+A)]$, $\epsilon_1=a_1(0)/a_2(0)$ and $\epsilon_3=a_3(0)/a_2(0)$. When $kh_a\to\infty$ or (and) $kh_b\to\infty$, the linear solutions (2.5)–(2.7) reduce to being applicable to the single-layer (semi-infinite) RMI. We note that the linear solutions (2.5)–(2.7) do not consider the effect of reverberating waves on the interfacial instabilities, which will further complicate the analysis and will be discussed later.

To eliminate the 2-D feature of the reverberating waves and validate the linear solutions by experiments, we further simplify the configuration by assuming that the exterior interfaces (i.e. the first and third interfaces) are initially unperturbed, i.e. $\epsilon_1=0$ and $\epsilon_3=0$ (see figure 2*b*). Then the linear solutions for this system reduce to

$$\dot{a}_1^l=\psi_1\dot{a}_2^R,\quad \dot{a}_2^l=\psi_2\dot{a}_2^R,\quad \dot{a}_3^l=\psi_3\dot{a}_2^R, \tag{2.8a–c}$$

with

$$\left.\begin{aligned}\psi_1 &= \frac{\xi_1[1-A-\alpha^2\beta^2(1+A)]-2\alpha\beta\xi_2}{A[\alpha^2\beta^2-1-\alpha\xi_1(\beta^2-1)-\beta\xi_2(\alpha^2-1)]},\\ \psi_2 &= \frac{A(\alpha^2\beta^2-1)+\alpha\xi_1(1+\beta^2)-\beta\xi_2(1+\alpha^2)}{A[\alpha^2\beta^2-1-\alpha\xi_1(\beta^2-1)-\beta\xi_2(\alpha^2-1)]},\\ \psi_3 &= \frac{2\alpha\beta\xi_1-\xi_2[A+1+\alpha^2\beta^2(1-A)]}{A[\alpha^2\beta^2-1-\alpha\xi_1(\beta^2-1)-\beta\xi_2(\alpha^2-1)]},\end{aligned}\right\} \tag{2.9}$$

and the Richtmyer growth rate (Richtmyer 1960) is

$$\dot{a}_2^R=Za_2(0)kA\Delta v_2. \tag{2.10}$$

Here Δv_2 is the jump speed of the second interface and the compression factor $Z=1-\Delta v_2/v_{TS_1}$, with v_{TS_1} the speed of the incident shock relative to the inner interface.

https://doi.org/10.1017/jfm.2021.903 Published online by Cambridge University Press

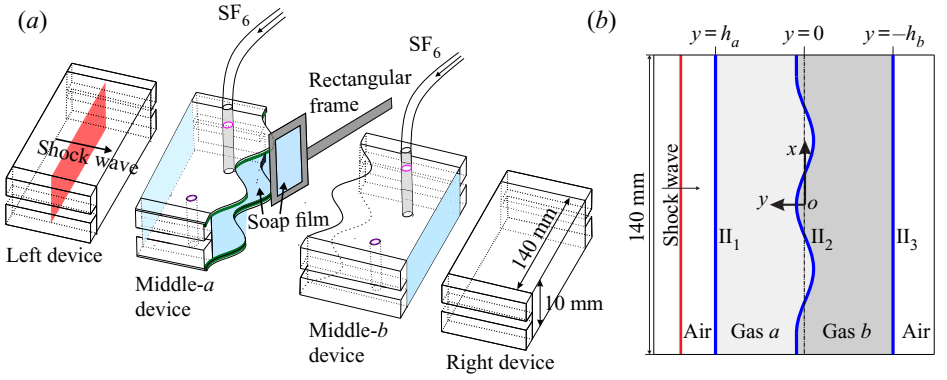


Figure 2. Schematics of (*a*) the soap-film interface generation and (*b*) the initial configuration. Here II_1, II_2 and II_3 denote the initial first, second and third interfaces, respectively.

If $A < 0$, (2.10) is replaced by the Meyer–Blewett growth rate (Meyer & Blewett 1972): $\dot{a}_2^R = (Z+1)a_2(0)kA\Delta v_2/2$. Although the exterior interfaces are initially unperturbed, the layer-coupling effect imposes the growth rates related to the inner interface on the exterior interfaces (see (2.8*a–c*)). Further, ψ_2 in (2.9) quantifies the layer-coupling effect on the inner interface. We note that the simplified configuration keeps all the essential physics such as the layer coupling, but greatly reduces the difficulty in experiment implementation and the non-uniformity of the flow between the layers.

3. Experimental method

Shock-tube experiments on such a simplified dual layer are performed in a horizontal shock tube with a 140 mm × 10 mm cross-sectional area to validate the simplified linear solutions (2.8*a–c*)–(2.10). First, the soap-film technique is utilised to generate shape-controllable and discontinuous quasi-2-D interfaces on the two sides of the middle-*a* device and the left side of the middle-*b* device, as shown in figure 2(*a*), mainly eliminating the additional short-wavelength perturbations, diffusion layer and three-dimensionality of the initial interfaces (Liu *et al.* 2018*a*; Liang *et al.* 2019). Then the air in the middle-*a* device and middle-*b* device is replaced by different volumes of SF_6. Finally, the left, middle-*a*, middle-*b* and right devices (see figure 2*a*) are combined and inserted in the shock tube, and the shock-tube experiments are conducted. Because the density of pure SF_6 is about five times that of air, it is reasonable to approximate the theoretical configuration with present experiments, although the dual layer is formed in the air, not a vacuum, in the experiments.

In the Cartesian coordinate system (indicated in figure 2*b*), the initial amplitude imposed on the inner interface is $a_2(0) = 2.0$ mm, and the wavenumber is $k = 104.7\ \mathrm{m}^{-1}$. The physical parameters of the dual-layer (i.e. cases D-L#LH and D-L#HL; 'D-L' represents dual layer; 'L', light; and 'H', heavy), single-layer (i.e. cases S-L#LH and S-L#HL; 'S-L' represents single layer) and semi-infinite (i.e. cases S-I#LH and S-I#HL; 'S-I' represents semi-infinite) interfaces are listed in table 1. Illuminated by a continuous light source (CEL-HXF300, maximum power output 249 W), the flow field is monitored by high-speed Schlieren photography. The frame rate of the high-speed video camera (FASTCAM SA5, Photron Ltd, with a sensor of 1024 pixels × 1024 pixels) is 60 000 frames per second with a shutter time of 1 μs. The spatial resolution of the Schlieren images is

https://doi.org/10.1017/jfm.2021.903 Published online by Cambridge University Press

Case	h_a	h_b	M	mf_a	mf_b	A	Δv_1	Δv_2	v_{TS_1}	v_{TS_2}	$\lvert\dot{\zeta}_2\rvert$	ψ_1	ψ_2	ψ_3
D-L#LH	25	25	1.20	0.81	0.90	0.22	82	74	236	190	1.20 ± 0.05	0.36	1.15	0.43
D-L#HL	25	25	1.20	0.90	0.37	−0.25	77	86	209	270	1.15 ± 0.05	0.39	1.13	0.34
S-L#LH	∞	25	1.20	0	0.90	0.57	—	77	413	209	1.05 ± 0.05	—	1.07	0.39
S-L#HL	25	∞	1.20	0.91	0	−0.58	76	97	205	407	1.05 ± 0.05	0.40	1.07	—
S-I#LH	∞	∞	1.20	0	0.89	0.55	—	78	413	214	1.0 ± 0.05	—	1	—
S-I#HL	∞	∞	1.25	0.87	0	−0.52	—	83	199	365	1.0 ± 0.05	—	1	—

Table 1. Physical parameters of gas layers: h_a and h_b are layer thicknesses; M denotes the incident shock Mach number; mf_a (mf_b) is the mass fraction of SF_6 in gas a (gas b); A denotes the Atwood number of the second interface; Δv_1 and Δv_2 denote the jump speed of the first and second interface, respectively; v_{TS_1} and v_{TS_2} denote the speed of the transmitted shock TS_1 and TS_2, respectively; $|\dot{\zeta}_2|$ denotes the dimensionless amplitude growth rate of the second interface measured from experiments; and ψ_1, ψ_2 and ψ_3 are dimensionless parameters calculated with (2.9). The units of thickness and speed are mm and m s^{-1}, respectively.

0.4 mm $pixel^{-1}$. In this study, the waves' displacements and speeds, and the amplitudes of the three interfaces, are measured from the Schlieren images. The measurement accuracies for the waves' speeds are 1 m s^{-1}, and for the waves' displacements and the interface amplitudes are 0.4 mm. The ambient pressure and temperature are 101.3 kPa and 299.5 ± 1.0 K, respectively. For each case, at least three experimental runs are performed, and the maximum variances from the mean for the inner interface amplitudes among diverse experimental runs are within 3 %.

4. One-dimensional motions of waves and interfaces

Owing to the different acoustic impedances of the various fluids in a dual layer, the reverberating waves inside the layers are multifarious. Based on the one-dimensional (1-D) gas dynamics theory (Drake 2018; Liang & Luo 2021), 1-D dimensionless t–y diagrams of the three interfaces and reverberating waves in cases D-L#LH and D-L#HL are shown in figures 3(a) and 3(b), respectively. Note that only significant waves for interface evolution are presented in the figures. The moment when the initial inner interface (II_2) is first shocked is defined as $t = 0$. Time is scaled as $\tau_{1D} = tv_{TS_1}/h_a$. Displacements of interfaces and waves are scaled as $\zeta_{1D} = y/h_a$.

In the D-L#LH case, after the incident shock first impacts the initial first interface (II_1), a transmitted shock (TS_1) is refracted inside gas a and moves towards the initial second interface (II_2). Second, after the TS_1 impacts the II_2, a transmitted shock (TS_2) is refracted inside gas b, and a reflected shock (RS) is generated and moves backwards, since the inner interface is a fast/slow one relative to the motion of TS_1. Third, after the RS impacts the shocked first interface (SI_1), the SI_1 decelerates, and rarefaction waves (RW_1) are reflected inside gas a, since the first interface is a slow/fast one relative to the motion of RS. Moreover, after the TS_2 impacts the initial third interface (II_3), a transmitted shock (TS_3) is refracted outside the layers, and rarefaction waves (RW_3) are reflected inside gas b, since the third interface is also a slow/fast one relative to the motion of TS_2. Fourth, the RW_1 impacts the shocked inner interface (SI_2), decelerating the SI_2 and refracting transmitted rarefaction waves (tRW_1) into gas b. Subsequently, the RW_3 impacts the SI_2, accelerating the SI_2 and refracting transmitted rarefaction waves (tRW_3) into gas a. Since the strength of the RW_3 is much larger than that of the RW_1, the final velocity of SI_2 is larger than the initial velocity jump induced by the TS_1. Fifth, the tRW_1 impacts and

https://doi.org/10.1017/jfm.2021.903 Published online by Cambridge University Press

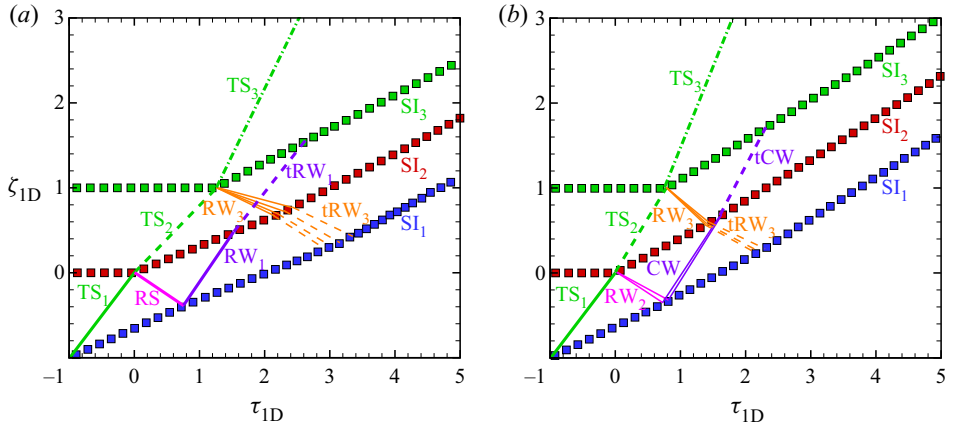


Figure 3. One-dimensional dimensionless t–y diagrams of a shocked dual layer in the (a) D-L#LH case and (b) D-L#HL case. TS, transmitted shock; RS, reflected shock; RW, rarefaction waves; tRW, transmitted rarefaction waves; CW, compression waves; tCW, transmitted compression waves; SI_1, SI_2 and SI_3, shocked first, second and third interface. Blue, red and green symbols represent the first, second and third interfaces' trajectories. Lines represent the waves' trajectories.

decelerates the shocked third interface (SI_3), and the tRW_3 impacts and accelerates the SI_1. Finally, all waves refract outside the dual layer, and the three interfaces move at the same speed.

In the D-L#HL case, after the TS_1 impacts the II_2, rarefaction waves (RW_2) are reflected inside gas a, since the inner interface is a slow/fast one relative to the motion of TS_1. Then, after the RW_2 impacts the SI_1, the SI_1 accelerates, and compression waves (CW) are reflected inside gas a, since the first interface is a slow/fast one relative to the motion of RW_2. Later, the CW impacts the SI_2, accelerating the SI_2 and refracting transmitted compression waves (tCW) into gas b. In addition, since the density gradient at the third interface is lower in the D-L#HL case on comparing with the D-L#LH case, the RW_3 in the D-L#LH case is stronger than that in the D-L#HL case.

5. Two-dimensional hydrodynamic instabilities

Schlieren images of the shock-induced evolutions of the dual-layer (three interfaces), single-layer (two interfaces) and semi-infinite (one interface) interfaces are shown in figure 4(a–f). In general, the waves in the 2-D case are similar to the 1-D counterparts and, therefore, we shall take the D-L#LH case as an example to discuss only the deformations of the three interfaces. First, after the TS_1 impacts the II_2 (46 μs), the rippled TS_2 is refracted inside gas b. Meanwhile, the perturbation on the inner interface grows gradually. Second, after the rippled TS_2 impacts the II_3, the II_3 is slightly deformed and the RW_3 impacts and accelerates the evolving SI_2 (212 μs). Third, after the RW_3 impacts the perturbed SI_2, rippled reverberating waves inside the two layers impact the nearly planar SI_1 and SI_3. Last, the three interfaces evolve with the same phase, and one can find that the largest perturbation is on the inner interface, and the smallest perturbation is on the third interface (912 μs).

The time-varying dimensionless amplitudes of the inner interface in three $A > 0$ cases (i.e. cases D-L#LH, S-L#LH and S-I#LH) and three $A < 0$ cases (i.e. cases D-L#HL, S-L#HL and S-I#HL) are measured and shown in figures 5(a) and 5(b), respectively.

https://doi.org/10.1017/jfm.2021.903 Published online by Cambridge University Press

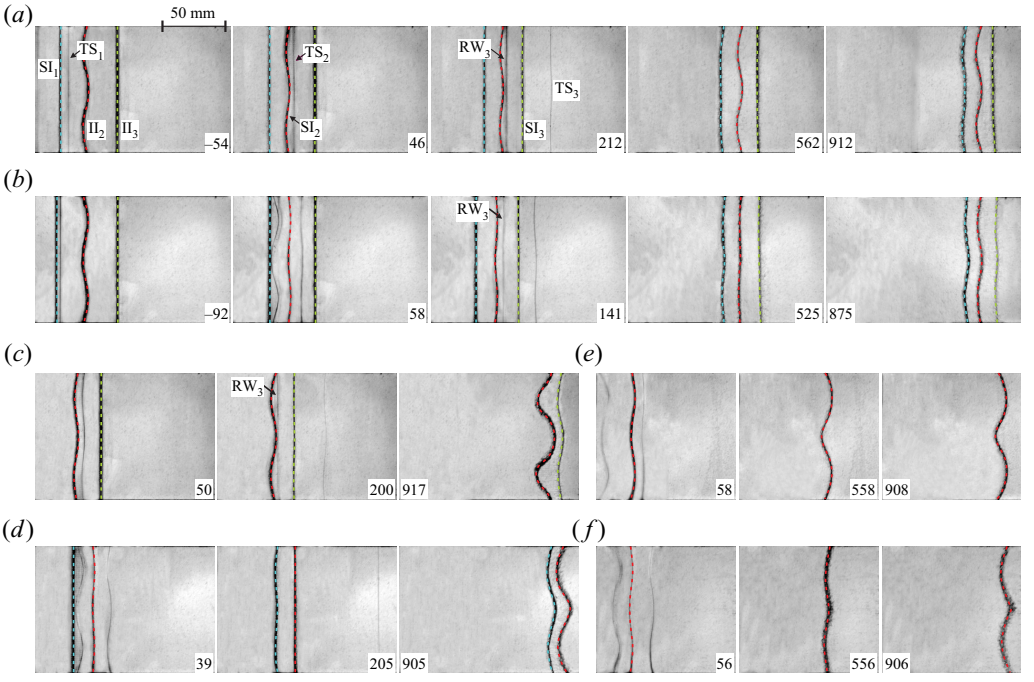


Figure 4. Schlieren images of shocked-layer evolutions in cases (*a*) D-L#LH, (*b*) D-L#HL, (*c*) S-L#LH, (*d*) S-L#HL, (*e*) S-I#LH and (*f*) S-I#HL. The first, second and third interfaces are marked with blue, red and green dashed lines, respectively. Numbers denote time in μs.

Time is scaled as $\tau_2 = k|\dot{a}_2^l|t$, and amplitude is scaled as $\zeta_2 = k(a_2 - Za_2(0))$. Here we calculate ψ_1, ψ_2 and ψ_3 using (2.9) by considering the shock compression on the initial layer thicknesses, i.e. $\alpha = \exp(-kZ_a h_a)$ and $\beta = \exp(-kZ_b h_b)$ with $Z_a = 1 - \Delta v_1/v_{TS_1}$ and $Z_b = 1 - \Delta v_2/v_{TS_2}$, where Δv_1 is the velocity jump at the first interface, and v_{TS_2} is the velocity of TS_2, respectively, as listed in table 1. The dimensionless amplitude growth rate ($|\dot{\zeta}_2|$) of the inner interface is obtained by linearly fitting the ζ_2 before the RW_3 impacts the inner interface, as listed in table 1. Before the RW_3 impacts the two interfaces (as marked with vertical dash-dotted lines), the good agreement between the ζ_2 with the predictions of linear solutions (as marked with black dashed lines with a slope of 1 for $A > 0$ cases or -1 for $A < 0$ cases) validates the established linear solutions. Likewise, the agreement between ψ_2 with $|\dot{\zeta}_2|$ in all cases also validates the linear solutions (see table 1). In addition, the ψ_2 in the $A > 0$ cases is larger than in the corresponding $A < 0$ cases. On the one hand, the phase reversal involved in the $A < 0$ cases enlarges the difference of the inner interface amplitude between $A > 0$ conditions and $A < 0$ conditions. On the other hand, the RW_3 is weaker in the $A < 0$ cases and induces less additional vorticity deposition on the inner interface (the effect of RW_3 will be discussed in detail later).

From (2.9), it is found that the layer-coupling effect is dependent only on kh_a, kh_b and A when $\epsilon_1 = \epsilon_3 = 0$. The variations of ψ_1, ψ_2 and ψ_3 versus A with $kh_a \in [0.1, 1.0, 10]$ and $kh_b \in [0.1, 1.0, 10]$ are calculated, as shown in figure 6. Four findings in particular are noteworthy. First, $\psi_2 > 1$, $\psi_1 > 0$ and $\psi_3 > 0$ in all cases, indicating that the layer-coupling effect leads to both the inner and exterior interfaces being more unstable. Second, smaller kh_a and kh_b lead to larger ψ_1, ψ_2 and ψ_3, indicating that thinner layers enhance the RMI more than thicker layers. Third, when A is fixed, ψ_2 for the condition

https://doi.org/10.1017/jfm.2021.903 Published online by Cambridge University Press

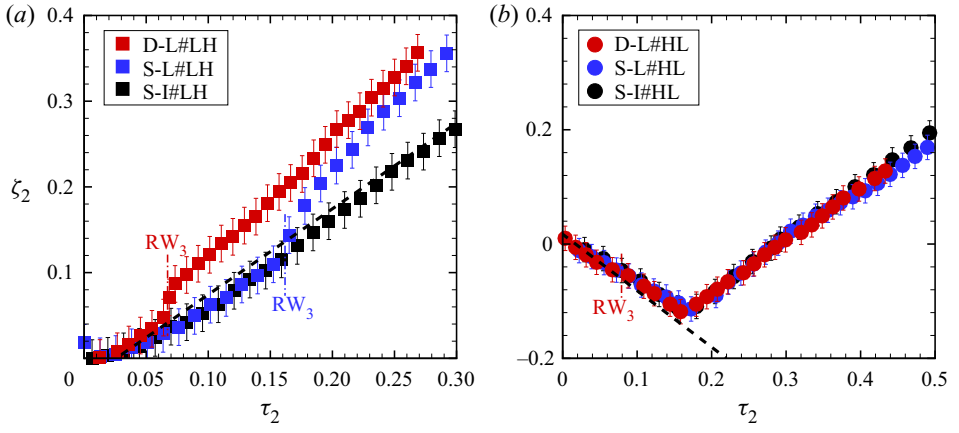


Figure 5. The dimensionless amplitudes of the inner interface for cases (*a*) D-L#LH, S-L#LH and S-I#LH, and (*b*) D-L#HL, S-L#HL and S-I#HL. The vertical dash-dotted lines represent the time when the RW_3 impacts the SI_2 in the corresponding colour case. Black dashed lines represent the linear solutions.

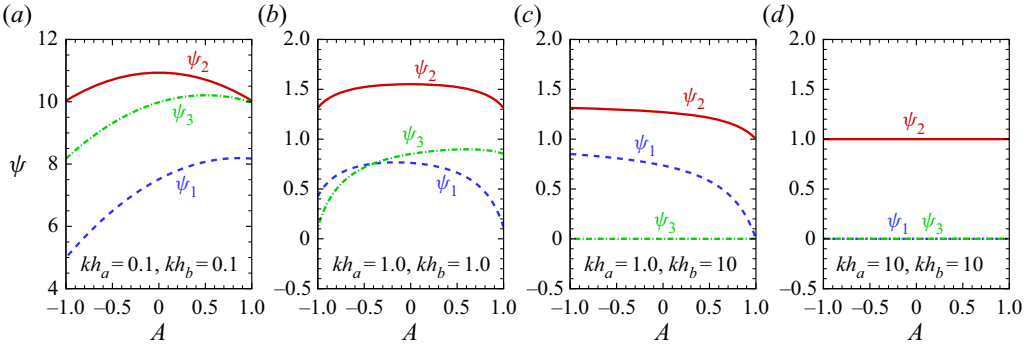


Figure 6. The variations of ψ_1, ψ_2 and ψ_3 versus A under conditions (*a*) $kh_a = 0.1$, $kh_b = 0.1$, (*b*) $kh_a = 1.0$, $kh_b = 1.0$, (*c*) $kh_a = 1.0$, $kh_b = 10$, and (*d*) $kh_a = 10$, $kh_b = 10$.

$kh_a = 1.0$ and $kh_b = 1.0$ is larger than ψ_2 for the condition $kh_a = 1.0$ and $kh_b = 10$, demonstrating that a dual layer enhances the RMI of the inner interface more than its single-layer counterpart. Fourth, if $kh_a < kh_b$ ($kh_a > kh_b$), ψ_2 for the $A = -1$ condition is larger (smaller) than those under the $A = 1$ condition, indicating that the influence of A on the layer-coupling effect is coupled with the relationship between the thicknesses of the two layers.

The reverberating waves inside layers are then considered. It is noted that the mechanisms of the influences of the layer coupling and the reverberating waves on the hydrodynamic instabilities are quite different. If there are no reverberating waves inside the layers, the layer coupling still influences the RMI of the three interfaces. The reverberating waves deposit additional vorticity on diverse interfaces and, therefore, induce additional instabilities on the three interfaces.

According to figure 5(*a*), the RW_3 dramatically changes the inner interface's instability development. First, the inner interface is a slow/fast one relative to the motion of RW_3 in cases D-L#LH and S-L#LH. Because of the baroclinic vorticity created by the misalignment of the density gradient ($\nabla\rho$) and the pressure gradient (∇p), the RW_3

https://doi.org/10.1017/jfm.2021.903 Published online by Cambridge University Press

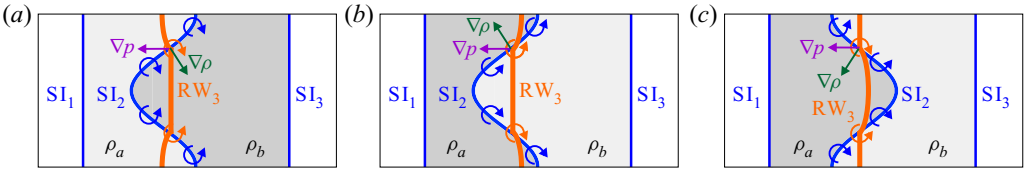


Figure 7. Sketches of the interaction of the RW_3 and SI_2 in cases (*a*) D-L#LH and S-L#LH, (*b*) D-L#HL when the time at which RW_3 impacts the inner interface (t_{RW_3}) is smaller than the end time of the inner interface's phase reversal (t_{ph}), and (*c*) D-L#HL when $t_{RW_3} > t_{ph}$. The RW_3 moves from right to left. The blue (orange) arcs with an arrow illustrate the vorticity deposition induced by the RW_3 on the inner interface. The purple (green) arrows represent the pressure (density) gradient ∇p ($\nabla \rho$).

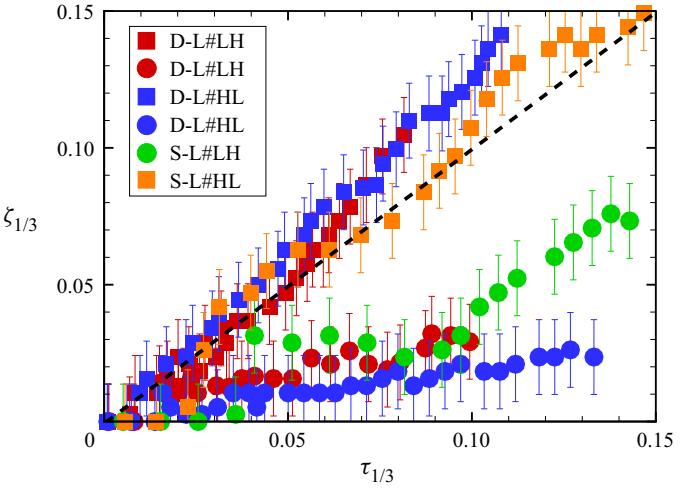


Figure 8. The time-varying amplitude growths of the first interface (square symbols) and third interface (circle symbols). The black dashed line represents the linear solutions.

continuously deposits vorticity with the same direction as the vorticity deposited by the TS_1 on the inner interface, as sketched in figure 7(*a*). As a result, the RW_3 induces an additional RTI on the inner interface and causes it to be more unstable than it would be without being affected by the RW_3. Second, although the inner interface is a fast/slow one relative to the motion of RW_3 in the D-L#HL case, the time when the RW_3 impacts the inner interface (t_{RW_3}) is smaller than the end time of the inner interface's phase reversal (t_{ph}) (see figure 5*b*). Consequently, the RW_3 induces an additional RTI on the inner interface and causes it to be more unstable than it would be without being affected by the RW_3 in this work, as sketched in figure 7(*b*). If h_b is larger and $t_{RW_3} > t_{ph}$, the RW_3 induces an additional Rayleigh–Taylor stabilisation on the inner interface and causes it to be more stable than it would be without being affected by the RW_3, as sketched in figure 7(*c*). Third, the approximate ζ_2 in cases S-L#HL and S-I#HL indicates that the reflected compression waves slightly influence the inner interface.

After the TS_1 impacts the perturbed inner interface, the reverberating waves become rippled. According to Ishizaki *et al.* (1996), the rippled reverberating waves seed small perturbations on the initially unperturbed exterior interfaces, and impose a gravitational instability driven by the acceleration induced by the rippled waves and the pressure perturbation behind them on the exterior interfaces. As a result, the perturbation growths of the initially unperturbed exterior interfaces are ascribed to the layer-coupling effect

https://doi.org/10.1017/jfm.2021.903 Published online by Cambridge University Press

and the instability driven by the rippled reverberating waves. The amplitudes of the exterior interfaces are measured from experiments, as shown in figure 8. For the first (third) interface, time is scaled as $\tau_1 = k\dot{a}_1^l t$ ($\tau_3 = k\dot{a}_3^l t$), and amplitude is scaled as $\zeta_1 = ka_1$ ($\zeta_3 = ka_3$). Both the ζ_1 and ζ_3 in all cases grow concussively, indicating the long-time influences of the reverberating waves on the two exterior interfaces' instabilities. Compared with the linear solutions (i.e. the black dashed line), it is found that ζ_1 is larger than the linear solutions but ζ_3 is smaller than the linear solutions, demonstrating that the reverberating waves promote the first interface development but inhibit the third interface development.

6. Conclusions

We propose a linear model to quantify the layer-coupling effect on the RMI of a dual layer. The layer-coupling effect is determined by the dimensionless thicknesses of the two layers, the amplitude ratios between exterior interfaces and the inner interface, and the Atwood number A of the inner interface. The model is validated through shock-tube experiments on dual-layer, single-layer and semi-infinite interface evolutions with the improved soap-film technique. It is noted that the differences between the model and experiment are due to the influence of reverberating waves and the influence of the non-vacuum conditions beyond the layers in the experiment. Assuming the exterior interfaces initially unperturbed, it is found that the layer-coupling effect destabilises all interfaces of a dual layer, especially when the layers are initially thin. Moreover, the layer-coupling effect on a dual layer is more vital than the single-layer counterpart. The influences of A and the relationship of the two layers' thicknesses on the layer-coupling effect are coupled. The reverberating waves between the layers induce additional instabilities on a dual layer, destabilising the inner interface and the first interface, but stabilising the third interface. These findings suggest that a slow/fast configuration with a large thickness in a dual layer can suppress the hydrodynamic instabilities relative to other dual-layer configurations. Therefore, the present study may be significant for understanding the complex interfacial instabilities and waves in an ICF capsule.

Acknowledgements. The authors appreciate the valuable suggestions of the reviewers.

Funding. This work was supported by Tamkeen under the NYU Abu Dhabi Research Institute grant CG002 and the Natural Science Foundation of China (nos 91952205 and 11625211).

Declaration of interests. The authors report no conflict of interest.

Author ORCIDs.
Yu Liang https://orcid.org/0000-0002-3254-7073;
Xisheng Luo https://orcid.org/0000-0002-4303-8290.

References

Balakumar, B.J., Orlicz, G.C., Ristorcelli, J.R., Balasubramanian, S., Prestridge, K.P. & Tomkins, C.D. 2012 Turbulent mixing in a Richtmyer–Meshkov fluid layer after reshock: velocity and density statistics. *J. Fluid Mech.* **696**, 67–93.

Brouillette, M. 2002 The Richtmyer–Meshkov instability. *Annu. Rev. Fluid Mech.* **34**, 445–468.

Budzinski, J.M., Benjamin, R.F. & Jacobs, J.W. 1994 Influence of initial conditions on the flow patters of a shock-accelerated thin fluid layer. *Phys. Fluids* **6**, 3510–3512.

Ding, J., Li, J., Sun, R., Zhai, Z. & Luo, X. 2019 Convergent Richtmyer–Meshkov instability of a heavy gas layer with perturbed outer interface. *J. Fluid Mech.* **878**, 277–291.

https://doi.org/10.1017/jfm.2021.903 Published online by Cambridge University Press

DRAKE, R.P. 2018 *High-energy-density physics: foundation of inertial fusion and experimental astrophysics*. Springer.

GONCHAROV, V.N. 1999 Theory of the ablative Richtmyer–Meshkov instability. *Phys. Rev. Lett.* **82** (10), 2091.

GUO, H.Y., WANG, L.F., YE, W.H., WU, J.F. & ZHANG, W.Y. 2017 Linear growth of Rayleigh–Taylor instability of two finite-thickness fluid layers. *Chin. Phys. Lett.* **34** (7), 075201.

HAINES, B.M., *et al.* 2021 Constraining computational modeling of indirect drive double shell capsule implosions using experiments. *Phys. Plasmas* **28** (3), 032709.

ISHIZAKI, R, NISHIHARA, K, SAKAGAMI, H & UESHIMA, Y 1996 Instability of a contact surface driven by a nonuniform shock wave. *Phys. Rev.* E **53** (6), R5592.

JACOBS, J.W., JENKINS, D.G., KLEIN, D.L. & BENJAMIN, R.F. 1995 Nonlinear growth of the shock-accelerated instability of a thin fluid layer. *J. Fluid Mech.* **295**, 23–42.

JACOBS, J.W., KLEIN, D.L., JENKINS, D.G. & BENJAMIN, R.F. 1993 Instability growth patterns of a shock-accelerated thin fluid layer. *Phys. Rev. Lett.* **70**, 583–586.

KURANZ, C.C., *et al.* 2018 How high energy fluxes may affect Rayleigh–Taylor instability growth in young supernova remnants. *Nat. Commun.* **9**, 1564.

LIANG, Y., LIU, L., ZHAI, Z., SI, T. & WEN, C.-Y. 2020 Evolution of shock-accelerated heavy gas layer. *J. Fluid Mech.* **886**, A7.

LIANG, Y. & LUO, X. 2021 On shock-induced heavy-fluid-layer evolution. *J. Fluid Mech.* **920**, A13.

LIANG, Y., ZHAI, Z., DING, J. & LUO, X. 2019 Richtmyer–Meshkov instability on a quasi-single-mode interface. *J. Fluid Mech.* **872**, 729–751.

LINDL, J., LANDEN, O., EDWARDS, J., MOSES, E. & TEAM, N. 2014 Review of the national ignition campaign 2009–2012. *Phys. Plasmas* **21**, 020501.

LIU, L., LIANG, Y., DING, J., LIU, N. & LUO, X. 2018*a* An elaborate experiment on the single-mode Richtmyer–Meshkov instability. *J. Fluid Mech.* **853**, R2.

LIU, W., LI, X., YU, C., FU, Y., WANG, P., WANG, L. & YE, W. 2018*b* Theoretical study on finite-thickness effect on harmonics in Richtmyer–Meshkov instability for arbitrary atwood numbers. *Phys. Plasmas* **25** (12), 122103.

MESHKOV, E.E. 1969 Instability of the interface of two gases accelerated by a shock wave. *Fluid Dyn.* **4**, 101–104.

MEYER, K.A. & BLEWETT, P.J. 1972 Numerical investigation of the stability of a shock-accelerated interface between two fluids. *Phys. Fluids* **15**, 753–759.

MIKAELIAN, K.O. 1985 Richtmyer–Meshkov instabilities in stratified fluids. *Phys. Rev. A* **31**, 410–419.

MIKAELIAN, K.O. 1993 Growth rate of the Richtmyer–Meshkov instability at shocked interfaces. *Phys. Rev. Lett.* **71** (18), 2903.

MIKAELIAN, K.O. 1996 Numerical simulations of Richtmyer–Meshkov instabilities in finite-thickness fluid layers. *Phys. Fluids* **8** (5), 1269–1292.

MILES, A.R., EDWARDS, M.J., BLUE, B., HANSEN, J.F., ROBEY, H.F., DRAKE, R.P., KURANZ, C. & LEIBRANDT, D.R. 2004 The effects of a short-wavelength mode on the evolution of a long-wavelength perturbatoin driven by a strong blast wave. *Phys. Plasmas* **11**, 5507–5519.

MONTGOMERY, D.S., *et al.* 2018 Design considerations for indirectly driven double shell capsules. *Phys. Plasmas* **25** (9), 092706.

ORLICZ, G.C., BALASUBRAMANIAN, S. & PRESTRIDGE, K.P. 2013 Incident shock mach number effects on Richtmyer–Meshkov mixing in a heavy gas layer. *Phys. Fluids* **25** (11), 114101.

OTT, E. 1972 Nonlinear evolution of the Rayleigh–Taylor instability of a thin layer. *Phys. Rev. Lett.* **29** (21), 1429.

PRESTRIDGE, K., VOROBIEFF, P., RIGHTLEY, P.M. & BENJAMIN, R.F. 2000 Validation of an instability growth model using particle image velocimetry measurement. *Phys. Rev. Lett.* **84**, 4353–4356.

QIAO, X. & LAN, K. 2021 Novel target designs to mitigate hydrodynamic instabilities growth in inertial confinement fusion. *Phys. Rev. Lett.* **126** (18), 185001.

RAYLEIGH, LORD 1883 Investigation of the character of the equilibrium of an incompressible heavy fluid of variable density. *Proc. London Math. Soc.* **14**, 170–177.

RICHTMYER, R.D. 1960 Taylor instability in shock acceleration of compressible fluids. *Commun. Pure Appl. Math.* **13**, 297–319.

RIGHTLEY, P.M., VOROBIEFF, P. & BENJAMIN, R.F. 1997 Evolution of a shock-accelerated thin fluid layer. *Phys. Fluids* **9** (6), 1770–1782.

SHARP, D.H. 1984 An overview of Rayleigh–Taylor instability. *Physica* D **12** (1), 3–18.

SUN, R., DING, J., ZHAI, Z., SI, T. & LUO, X. 2020 Convergent Richtmyer–Meshkov instability of heavy gas layer with perturbed inner surface. *J. Fluid Mech.* **902**, A3.

TAYLOR, G. 1950 The instability of liquid surfaces when accelerated in a direction perpendicular to their planes. I. *Proc. R. Soc. Lond.* A **201** (1065), 192–196.

https://doi.org/10.1017/jfm.2021.903 Published online by Cambridge University Press

TOMKINS, C., KUMAR, S., ORLICZ, G. & PRESTRIDGE, K. 2008 An experimental investigation of mixing mechanisms in shock-accelerated flow. *J. Fluid Mech.* **611**, 131–150.

ZHAI, Z., ZOU, L., WU, Q. & LUO, X. 2018 Review of experimental Richtmyer–Meshkov instability in shock tube: From simple to complex. *Proc. Inst. Mech. Eng.* C **232**, 2830–2849.

ZHOU, Y. 2017*a* Rayleigh–Taylor and Richtmyer–Meshkov instability induced flow, turbulence, and mixing. I. *Phys. Rep.* **720-722**, 1–136.

ZHOU, Y. 2017*b* Rayleigh–Taylor and Richtmyer–Meshkov instability induced flow, turbulence, and mixing. II. *Phys. Rep.* **723–725**, 1–160.

ZHOU, Y., CLARK, T.T., CLARK, D.S., GLENDINNING, S.S., SKINNER, A.A., HUNTINGTON, C., HURRICANE, O.A., DIMITS, A.M. & REMINGTON, B.A. 2019 Turbulent mixing and transition criteria of flows induced by hydrodynamic instabilities. *Phys. Plasmas* **26** (8), 080901.

https://doi.org/10.1017/jfm.2021.903 Published online by Cambridge University Press